Computational and theoretical study of the Coandă effect

Author: Joel Conejero Frechilla
Facultat de Física, Universitat de Barcelona, Diagonal 645, 08028 Barcelona, Spain.

Advisor: David Reguera López

Abstract: This work explores the Coandă effect through both theoretical analysis and computational simulations. A theoretical framework is first developed to understand the physical principles underlying the phenomenon. Then, Computational Fluid Dynamics (CFD) simulations are carried out to visualize and quantify the effect in two distinct configurations. The first scenario considers a jet impinging on a cylindrical object at various vertical positions, to demonstrate the existence of a restoring force. The second examines the influence of the velocity when an inlet is placed on top of the cylinder to analyze the deflection angle. Simulations are conducted in both laminar and turbulent flow regimes to assess the consistency of the observed behavior. These findings highlight the practical relevance of the Coandă effect in flow control and lift generation, with applications in aerospace and fluidic device design.
Keywords: Coandă effect, CFD, simulation, Navier-Stokes equations, Reynolds number
SDGs: 3, 6, 7, 9, 12, 13

I. INTRODUCTION

Everyone has, at some point, spilled their coffee or water while trying to pour it from a glass. The liquid seems to have a strange tendency to cling to the lip and flow down the side instead of going where you want it to. Fortunately—there's a physical explanation behind all those coffee stains!

Back in 1910, a Romanian engineer named Henri Coandă was testing a new type of flying machine he had designed, the *Coandă-1910.* Although he didn't manage to get it flying successfully, something unexpected happened during the test. Coandă, concerned that the hot exhaust from the engine might damage the fuselage, added metal plates to deflect the flames away from the aircraft. However, when he powered up the engine, he observed something surprising: instead of pushing the flames away, the plates seemed to cause the exhaust to stick to the fuselage! Astonished by this behavior, and with the help of the physicist Theodore von Kármán, he realized he had stumbled upon a new aerodynamic phenomenon—what we now call the Coandă effect [1][2].

Since then, the Coandă effect has found numerous practical applications, from enhancing lift in aircraft wings [3] and powering micro air vehicles (MAVs) [4], to enabling no-tail-rotor helicopters like the NOTAR [5]. It has even been applied in everyday contexts like room ventilation [6] and hair dryers.

This paper aims to explore the physics of the Coandă effect through both theoretical analysis and computational simulations. Specifically, we study the behavior of a jet stream as it interacts with a cylindrical obstacle—–a simple experiment that can even be replicated at home or be seen at the "L'ou com balla", a tradition in Catalonia which an egg is introduced in a water fountain and "dances" as it levitates.

II. THEORETICAL FRAMEWORK

Consider a jet of air at constant speed with curved streamlines resulting from its interaction with a cylindrical object [7], as shown in Fig. 1.

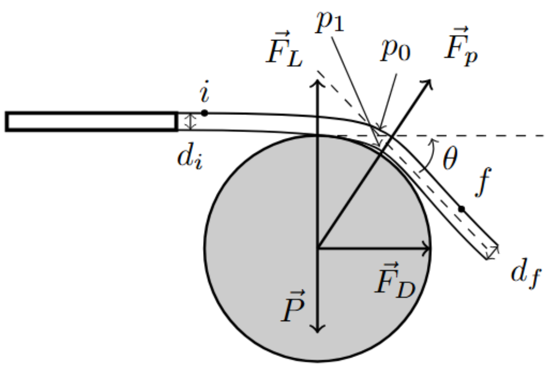

FIG. 1: A jet of air deflected by encountering a cylindrical object in its path.

Assuming negligible viscous friction and volume forces, we start with the Euler equation for an incompressible, steady flow:

$$\rho \left(\vec{v} \cdot \vec{\nabla} \right) \vec{v} = -\vec{\nabla} p. \tag{1}$$

In cylindrical coordinates, projecting along the radial direction and evaluating the scalar product leads to:

$$\frac{\partial p}{\partial r} = \rho \frac{v_\theta^2(r)}{r}. \tag{2}$$

Equation (2) shows that pressure increases with the radial distance from the center of curvature of the streamlines. This implies that, near the surface of the cylindrical object, where the radius of curvature is smaller, the pressure is lower, i.e., $p_1 < p_0$.

This pressure gradient is central to the explanation of the Coandă effect. When a jet of air flows near a convex surface (such as a ball or cylinder), it tends to remain attached to the surface due to the curvature of the streamlines; a reduced pressure region is created on the side where the flow is deflected, as indicated by Eq. (2).

Since the fluid is incompressible, the continuity equation in 2D implies that $v_i d_i = v_f d_f$, where d_j $(j = i, f)$ is the thickness of the jet at the initial and final point, where the deflected streamline detaches from the object, respectively. This allows us to apply Bernoulli's equation

$$p_i + \frac{1}{2}\rho v_i^2 = p_a + \frac{1}{2}\rho v_f^2, \tag{3}$$

where p_i is the pressure at the initial point and p_a is the atmospheric pressure. From Eq. (3), and assuming $p_i = p_a$, we deduce that $v_i = v_f$, and therefore, from continuity, $d_i = d_f$.

Applying the conservation of linear momentum to the control volume bounded by the jet, we obtain the following.

$$\vec{F}_p = \rho v_i^2 d_i \hat{e}_i - \rho v_f^2 d_f \hat{e}_f. \tag{4}$$

Here, $\vec{F}_p$ is the net pressure-induced force acting on the object, and $\hat{e}_i$ and $\hat{e}_f$ are the unit vectors in the direction of the initial and final velocity of the jet, respectively. Taking into account that $v_i = v_f$ and $d_i = d_f$, and using $\hat{e}_i = (1, 0)$ and $\hat{e}_f = (\cos\theta, -\sin\theta)$, we can express the equations in the x and y component:

$$F_{p_x} = \rho v_i^2 d_i (1 - \cos\theta) \tag{5}$$

$$F_{p_y} = \rho v_i^2 d_i \sin\theta. \tag{6}$$

Finally, one can obtain the modulus of the net applied force in terms of the angle of deflection θ:

$$F_p = \rho v_i^2 d_i \sqrt{2(1 - \cos\theta)}. \tag{7}$$

This expression quantitatively relates the magnitude of the Coandă-induced lateral force to the observable curvature of the air jet in the limit of an incompressible fluid.

III. COMPUTATIONAL METHODOLOGY

In order to adress this problem beyond the ideal fluid approximation, a CFD model was implemented using Siemens STAR-CCM+ 2019, a software that numerically solves the Navier–Stokes equations using a finite-volume approach. The computational domain is discretized into a mesh composed of small control volumes (cells), over which the governing equations are solved simultaneously. To ensure reliable and accurate results, a mesh convergence study was conducted prior to running the simulations. This step is crucial to guarantee that the numerical solution does not depend on the mesh resolution.

STAR-CCM+ provides a wide range of laminar and turbulent flow regimes. The appropriate model is selected based on the Reynolds number, defined as:

$$Re = \frac{\rho u L}{\mu}, \tag{8}$$

where ρ is the fluid density, u the characteristic velocity, L the characteristic length scale, and μ the dynamic viscosity. Flows with $Re < 2000$ are typically classified as laminar, characterized by smooth, parallel streamlines and low mixing. At higher Reynolds numbers, the flow becomes turbulent, exhibiting chaotic velocity fluctuations and enhanced mixing.

For the laminar regime, the governing Navier-Stokes equations reflect the conservation of mass and momentum. In this work, the flow is modeled as an incompressible fluid with constant density and restricted to a two-dimensional geometry. Under these assumptions, the governing equations simplify to:

1. Continuity equation (mass conservation):

$$\frac{\partial u_x}{\partial x} + \frac{\partial u_y}{\partial y} = 0 \tag{9}$$

2. Momentum equation:

$$\rho\left(\frac{\partial u_i}{\partial t} + u_x\frac{\partial u_i}{\partial x} + u_y\frac{\partial u_i}{\partial y}\right) = -\frac{\partial p}{\partial x_i} + \mu\left(\frac{\partial^2 u_i}{\partial x^2} + \frac{\partial^2 u_i}{\partial y^2}\right) \tag{10}$$

where $i = x, y$.

For the turbulent regime, we used the Spalart-Allmaras Model (*Appendix A*).

The computational approach presented in this section aims to investigate two distinct effects related to the Coandă phenomenon. The first study focuses on the existence of a restoring force acting on a spherical object placed within a jet stream. The second study examines how a jet is deflected when it is directed near a convex surface. Both configurations are designed to illustrate the influence of surface curvature on the behavior of the jet. For both studies, the cylinder radius is $R = 2$ cm, which is the typical value for a ping-pong ball. The Spalart-Allmaras turbulence model was used as it gives the best convergences results.

A. First study

In the first scenario (see Fig. 2), an inlet was placed within a tube of length $L = 4$ cm and thickness $h = 0.2$ cm. The tube was located at a horizontal distance $b_x = -3.5$ cm from the origin, taken at the center of the circle. The tube was then displaced vertically above and below the horizontal axis to analyze how the path of the jet was altered depending on the vertical distance b_y from the center of the circle. For each position, simulations were run with different input velocities.

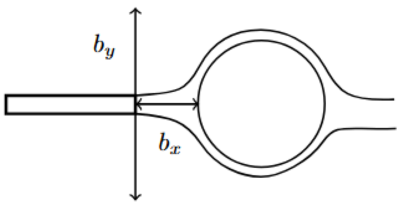

FIG. 2: Graphical representation of the 1st scenario.

The mesh (shown in Fig. 3) was refined on the most important part of the geometry. It was determined that the most suitable option was to use 15 Prism Layers with a 1.2 stretching factor. Also, the circumjacent region was refined with a finer mesh to ensure a good resolution of the equations in that area. The number of iterations used to solve the time-dependent equations where around 20000 (20s in physical time).

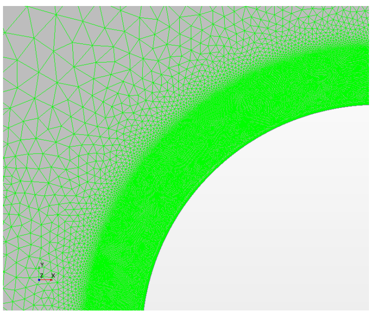

FIG. 3: Detail of the mesh grid near the circle.

B. Second study

In the second scenario, a small inlet of width h was placed at coordinates $(0, R)$ cm relative to the origin. Various inlet widths and velocities were tested in this configuration to determine how the deflection angle depends on these conditions.

For this case, the mesh was made from a Quadrilateral Mesher as it is better for a radial distribution. This

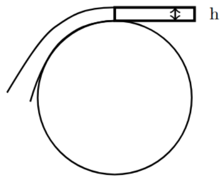

FIG. 4: Graphical representation of the 2nd scenario.

choice has allowed to improve the computational time maintaining a robust and converged solution. As the model used is unsteady, we simulated 6 s of physical time (with a 10^{-3} s time step) to ensure a good convergence of the results.

IV. RESULTS AND DISCUSSION

A. First Study

The objective of this study was to analyze the drag and lift forces and coefficients as a function of the vertical position of the jet relative to the cylindrical object for different Reynolds numbers. In this case, as all $Re > 1 \cdot 10^4$, a turbulent model was used.

The tested inlet velocities were $v = 5$, 10, 15, and 20 m/s, that correspond to typical values of human blowing.

The lift (L) and drag (D) coefficient are computed through the following equation:

$$C_{L,D} = \frac{F_{L,D}}{\frac{1}{2}\rho A v^2} \tag{11}$$

where F_L and F_D are the lift (i.e vertical component) and drag (i.e horizontal component) forces, "A" is the section area, ρ the air density and v, the air velocity.

From the results plotted in Figs. 5 and 6 (with a typical value of the lift and drag forces in the range of $1 \cdot 10^{-2} - 1$ N), it can be observed that the drag coefficient is symmetric, reaches its minimum when the jet is aligned with the center of the cylinder, and hits its maximum at $1.5 < b_y < 1.75$ cm. As for the lift coefficient, it is also symmetrical and changes to negative at zero, indicating a restoring type force. It is also shown that the lift coefficient is maximum at the same point as the drag coefficient. Moreover, if $b_y = R$, the jet no longer attaches to the cylinder, which causes a low drag/lift coefficient, except for the case of $Re = 5.3 \cdot 10^4$, where the jet is still attached. As for the $Re = 1.3 \cdot 10^4$ case, small vortices were generated between the inlet tube and the cylinder, which caused the different behavior observed in Figs. 5 and 6.

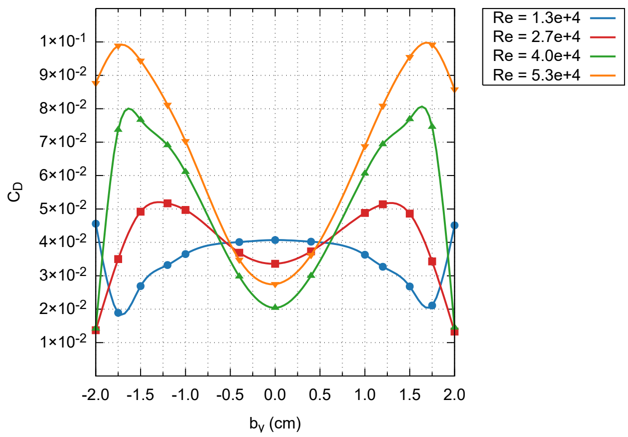

FIG. 5: Graphical representation of the drag coefficient obtained as a function of the vertical parameter b_y.

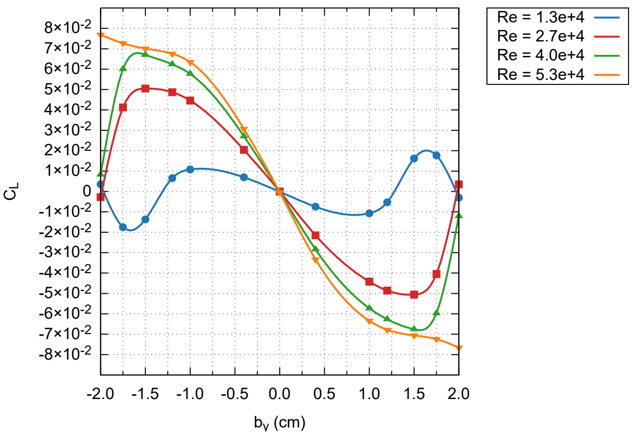

FIG. 6: Graphical representation of the lift coefficient obtained as a function of the vertical parameter b_y.

The behavior shown in both figures is a direct consequence of the Coandă effect, which causes the airflow to attach and curve around the surface. When the flow deviates more to one side, the pressure difference induces a lateral force that restores the ball to the jet centerline, allowing it to remain suspended.

Increasing the inlet velocity amplifies both drag and lift forces. For comparison, a ping-pong ball with mass 2.7 g has a weight of $P = 2.65 \cdot 10^{-2}$ N. In the case of $Re = 4 \cdot 10^4$, the simulated drag force is $F_D = 0.27$ N, which is sufficient to counteract gravity and generate enough force to support the ball.

B. Second Study

In this study, simulations were conducted at various velocities covering the laminar, transitional, and turbulent regimes. Prior to the full analysis, the model was verified by reproducing the results from [8] with the same configuration, confirming its validity.

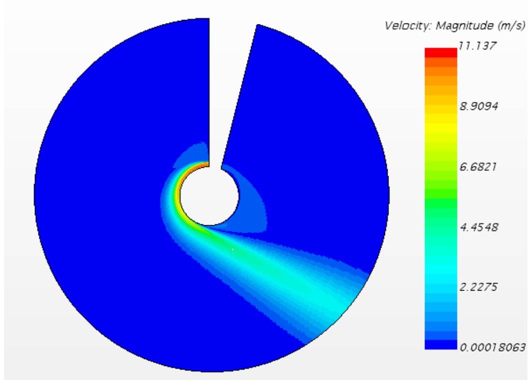

FIG. 7: Velocity profile for $v = 10$ m/s where the deflection of the jet due to the Coandă effect is clearly visible.

Plotting the deflection angle as a function of the Reynolds number reveals that higher velocities result in greater deflection. Simulations were also performed for different inlet thicknesses, with $h = 0.3$ cm found to be the most suitable for clearly demonstrating the Coandă effect. The study showed that increasing the inlet thickness significantly reduces the deflection angle. Moreover, on Fig. 8, from $Re = 10^3$ to $Re = 10^4$, the growth follows a logarithmical increase $y = 70.60 \cdot \ln(x) - 385.30$.

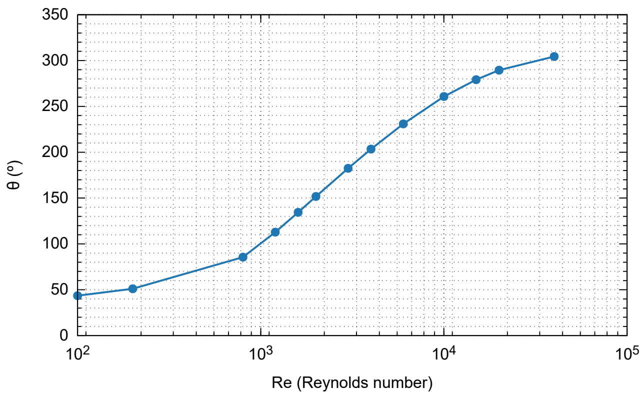

FIG. 8: Semi-logarithmic plot of the deflection angle θ as a function of the Reynolds number for an inlet thickness of $h = 0.3$ cm.

Another relevant aspect is the analysis of the lift coefficient plotted in Fig. 9. There exists a threshold value at which the lift coefficient becomes negative, occurring when $\theta > 180°$. This transition takes place in the range $2000 < Re < 3000$ (i.e., for $10 < v < 15$ m/s). A negative lift coefficient implies that the flow exerts a downward force on the circular body.

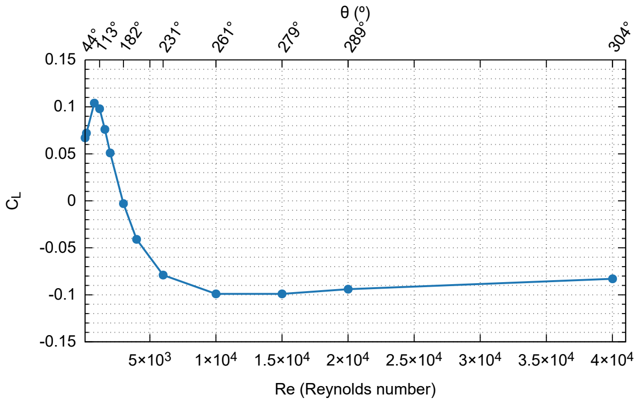

FIG. 9: Lift coefficient as a function of the Reynolds number.

Additionally, the CFD results can be compared with the theoretical predictions for the force discussed in Section II (see Eq. 7).

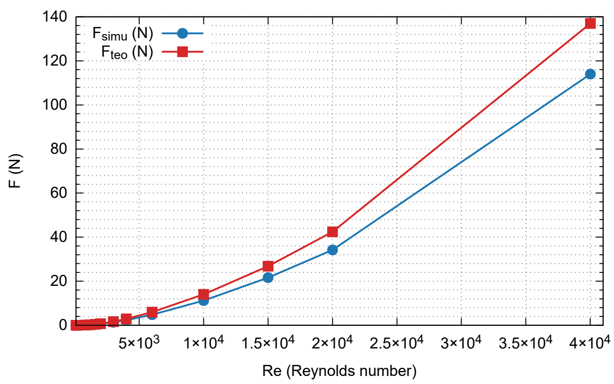

FIG. 10: Comparison of theoretical and simulated results for the modulus of the force for various inlet velocities.

As seen in Fig. 10, the theoretical and simulated results exhibit a similar trend, validating the theoretical approach developed in Section II.

V. CONCLUSIONS

The objective of this work was to analyze two distinct phenomena associated with the Coandă effect. The first study investigated the presence of a restoring force acting on a circular object placed within a jet stream. The second study examined the deflection of a jet when it is directed near a convex surface.

In the first case, the lift coefficient exhibits a restoring-type behavior, increasing as the ball moves away from the jet centerline and acting to pushing back toward the center. This effect is caused by the pressure reduction induced by the flow curvature around the object. As a result, the ball tends to remain within the jet stream, as famously demonstrated in the "L'ou com ball" spectacle. Additionally, the drag coefficient decreases as the lateral position b_y of the ball approaches the centerline, where the flow is more aligned with the object and resistance is minimized.

In the second case, increasing the Reynolds number led to a greater deflection angle of the jet that can surpsingly exceed 180° when $Re \geq 5 \cdot 10^4$. Additionally, the forces obtained in the simulation for a real fluid were compared with the theoretical estimate for an ideal fluid, showing a qualitative agreement between both.

The lift and drag forces analyzed in this work and generated by the Coandă effect can be used in practical applications ranging from aerospace to industrial fluid control. Future studies could explore the Coandă effect in 3D or over airfoils or non-symmetrical shapes.

Acknowledgments

I would like to express my sincere gratitude to my advisor, Dr. David Reguera López, for his guidance and patience throughout this project. I also wish to thank the Aerodynamics Department at e-Tech Racing for providing the necessary tools and support for the simulations.

[1] D.J. Piñeiro. "Henry Marie Coandă y el efecto 'Coandă'". Archivos de Cardiología de México, 2010, p.48-51.
[2] I. Reba. "Applications of the Coandă effect". Scientific American, 1996, Vol.214, No.6, p.84-93.
[3] H. Djojodihardjo et al. "Numerical simulation and analysis of Coandă effect circulation control for wind-turbine application considerations". IIUM Engineering Journal, Special Issue, Mechanical Engineering, 2011.
[4] H. Djojodihardjo and R.I. Ahmed. "Analtyical, Computational Fluid Dynamics and Flight Dynamics of Coandă MAV". IOP Conf. Ser.: Mater. Sci. Eng., 2016.
[5] I. Cîrciu and M. Boşcoianu. "An analysis of the efficiency of Coandă - NOTAR anti-torque systems for small helicopters". INCAS BULLETIN, 2010, Vol.2, No.4, p.81-88.
[6] A. Li. "Extended Coandă Effect and attachment ventilation". Indoor and Built Enviroment, 2019, Vol.28, No.4, p.437-442.
[7] E. Guyon. "Physical Hydrodynamics". Oxford University, 2001, p.187-189
[8] M. Subhash and A. Dumas. "Computational Study of Coanda Adhesion Over Curved Surface". SAE International Journal of Aerospace, 2013.

Estudi teòric i computacional de l'efecte Coandă

Author: Joel Conejero Frechilla
Facultat de Física, Universitat de Barcelona, Diagonal 645, 08028 Barcelona, Spain.

Advisor: David Reguera López

Resum: Aquest treball explora l'efecte Coandă mitjançant una anàlisi teòrica i simulacions computacionals. En primer lloc, es desenvolupa un marc teòric per comprendre els principis físics que expliquen el fenomen. A continuació, es duen a terme simulacions de Dinàmica de Fluids Computacional (CFD) per visualitzar i quantificar l'efecte en dues configuracions diferents. El primer escenari considera un raig que impacta sobre un objecte cilíndric en diverses posicions verticals. El segon analitza la influència de la velocitat quan una entrada de flux es col·loca a la part superior del cilindre per estudiar l'angle de deflexió. Les simulacions es realitzen tant en règim laminar com turbulent per avaluar la coherència del comportament observat.
Paraules clau: Efecte Coandă, CFD, simulació, equacions de Navier-Stokes, nombre de Reynolds
ODSs: 3, 6, 7, 9, 12, 13

Objectius de Desenvolupament Sostenible (ODSs o SDGs)

1. Fi de les desigualtats		10. Reducció de les desigualtats	
2. Fam zero		11. Ciutats i comunitats sostenibles	
3. Salut i benestar	X	12. Consum i producció responsables	X
4. Educació de qualitat		13. Acció climàtica	X
5. Igualtat de gènere		14. Vida submarina	
6. Aigua neta i sanejament	X	15. Vida terrestre	
7. Energia neta i sostenible	X	16. Pau, justícia i institucions sòlides	
8. Treball digne i creixement econòmic		17. Aliança pels objectius	
9. Indústria, innovació, infraestructures	X		

Appendix A: Spalart-Allmaras Turbulence Model (STAR-CCM+)

The simulation was performed using the following configuration:

- Two-dimensional (2D) domain
- Unsteady flow (Implicit Unsteady)
- Constant density gas
- Segregated flow solver
- Turbulent regime using the Spalart-Allmaras model
- All y^+ Wall Treatment

The governing equations solved by STAR-CCM+ under these conditions are described below.

1. Continuity Equation (Mass Conservation)
For incompressible (constant-density) flow:

$$\nabla \cdot \vec{u} = 0 \tag{A1}$$

2. Momentum Equation (RANS Form)
The Reynold-Averaged Navier-Stokes (RANS) form refers to a time-averaged version of the equations. Instead of resolving all instantaneous fluctuations, the RANS equations describe the mean flow behavior.

$$\rho\left(\frac{\partial \vec{u}}{\partial t} + \vec{u}\cdot\nabla\vec{u}\right) = -\nabla p \tag{A2}$$
$$+\nabla\cdot(\mu+\mu_t)\left(\nabla\vec{u}+\nabla\vec{u}^T\right)\big]$$

Where:

- $\vec{u}$: velocity vector
- μ: molecular viscosity
- μ_t: turbulent (eddy) viscosity
- ρ: fluid density

3. Spalart-Allmaras Turbulence Model
The Spalart-Allmaras model solves a single transport equation for a modified turbulent viscosity $\tilde{\nu}$:

$$\begin{aligned}\frac{\partial\tilde{\nu}}{\partial t} + \vec{u}\cdot\nabla\tilde{\nu} = C_{b_1}(1-f_{t_2})S\tilde{\nu} \\ + \frac{1}{\sigma}\left[\nabla\cdot((\nu+\tilde{\nu})\nabla\tilde{\nu}) + C_{b_2}(\nabla\tilde{\nu})^2\right] \\ - \left[C_{w_1}f_w - \frac{C_{b_1}}{\kappa^2}f_{t_2}\right]\left(\frac{\tilde{\nu}}{d}\right)^2\end{aligned} \tag{A3}$$

Where:

- $\tilde{\nu}$: modified turbulent viscosity
- d: distance to the nearest wall
- S: magnitude of vorticity
- f_{t_2}, f_w: model damping functions
- $C_{b_1}, C_{b_2}, C_{w_1}, \sigma, \kappa$: empirical constants

The actual turbulent viscosity is computed as:

$$\nu_t = \tilde{\nu} f_{v_1}, \quad \text{where} \quad f_{v_1} = \frac{\chi^3}{\chi^3 + C_{v_1}^3}, \quad \chi = \frac{\tilde{\nu}}{\nu} \tag{A4}$$

4. Wall Treatment

The All y^+ wall treatment is used to allow both fine and coarse near-wall mesh resolutions, blending wall function and low-Reynolds number approaches automatically.

5. Time Integration Scheme

The simulation uses an implicit unsteady method, which integrates the time-dependent terms as:

$$\frac{\partial\phi}{\partial t} \approx \frac{\phi^{n+1}-\phi^n}{\Delta t} \tag{A5}$$

This approach is unconditionally stable and suitable for large time steps.

6. Numerical Solver Configuration

To solve the discretized equations, STAR-CCM+ uses the SIMPLE (Semi-Implicit Method for Pressure-Linked Equations) algorithm for pressure-velocity coupling in the segregated flow solver. This iterative method updates the velocity and pressure fields to ensure mass conservation through the continuity equation.

For the linear systems involved in the pressure correction step, the default PARDISO direct solver was used, offering robust and efficient performance for both steady and unsteady simulations.